Assessing the dynamics of hemithioindigo-based photoswitches using multi-state molecular mechanics

Elias Harrer[1,2], Carolin Müller[2], Henry Dube[3], Dirk Zahn[1,2*]

[1] *Chair of Theoretical Chemistry, Friedrich-Alexander-Universität Erlangen-Nürnberg, Egerlandstraße 3, 91058 Erlangen, Germany*

[2] *Computer Chemistry Center, CCC, Friedrich-Alexander-Universität Erlangen-Nürnberg, Nägelsbachstraße 25, 91052 Erlangen, Germany*

[3] *Chair of Organic Chemistry I, Friedrich-Alexander-Universität Erlangen-Nürnberg, Nikolaus-Fiebiger-Str. 10, 91058 Erlangen, Germany*

*corresponding author: dirk.zahn@fau.de

Abstract:

We outline a multi-state molecular mechanics model for describing hemithioindigo-based photoswitches in the ground and excited (S_1) states, respectively. While retaining near quantum mechanical accuracy of the related Born-Oppenheimer potential energy profiles, the computational efficiency of our approach offers ns-scale molecular dynamics simulation runs featuring extended statistics of complex systems. Contrasting a series of different environments, we elucidate the explicit solvent effect on photoinduced *Z-E* switching in terms of both energetics and kinetic aspects. Using thousands of trajectories, isomerization ratios and relaxation times are directly assessed from statistical sampling. On this basis, in-depth mechanistic understanding is achieved via trajectory committor analyses that unravel the key descriptors of the *Z-E* isomerization process.

Keywords: hemithioindigo, photoswitches, multi-state molecular mechanics, committor analysis

Introduction:

Photoswitches, e.g. molecules that undergo reversible changes in their structure and properties upon irradiation with light, offer promising opportunities of steering the conversion of optical- into mechanical energy through powered nanoscale motions. In particular, the combination of photoswitching with controlled directional motion, referred to as light-driven molecular motors,[1–3] enables fascinating prospects in nanotechnology and molecular engineering. Notable examples of photoswitch-driven nanodevices and molecular machines include the light-control of surface wettability,[4,5] optoelectronics such as light-powered electrical switches,[6] chemical sensing,[7,8] and photosensitive medicine.[9–11] Especially for biological- and material science applications that do not tolerate high-energy input, the absorption of visible light by the photoswitchable chromophores is particularly desirable.[9,12–17]

Apart from the long-known azobenzenes, a recently emerging class of photoswitches is given by indigoids[18,19] and particularly hemithioindigo (HTI) (Scheme 1).[20] These compounds feature such desired low-energy absorption bands for electronic excitations together with a good thermal bi-stability, and chemical durability along the switching process.[20,21] Consequentially, HTIs have found their way into a plethora of applications including molecular machines such as motors,[3,22,23] gears,[24,25] or tweezers,[26] as well as photoresponsive catalysis,[27] supramolecular chemistry,[28–30] molecular computing,[31,32] or photopharmacology.[33–36] Further chemical modifications have been employed to enable HTI attachment to metal surfaces,[37] or to tailor self-assembly.[38,39]

The photoreactions of hemithioindigo-based molecules were extensively studied in the past by both, experimental[40–47] and theoretical investigations[48–51]. In the most straight-

forward cases, these molecules undergo torsional deformation of the double bond upon visible light excitation, and thus form Z and E isomers after relaxation to the electronic ground state. However, more complex bond rotations of HTIs in the excited state have also been developed recently, notably concomitant single and double bond rotation as initially propsed by Liu and Asato,[52] the Hula Twist photoreaction,[53] or a single bond rotation.[54] Moreover, the kinetics and type of photoreaction depends on the specific environment, such as the choice of the solvent.[42–44]

Both, the groups of *de Vivie-Riedle*[49] and *Maurer*[51] found that the photoinduced double-bond isomerization (DBI) in unsubstituted hemithioindigo (scheme 1) is largely characterized by dihedral rotation around the central -C=C- bond. Moreover, depending on stilbene substitution, the molecule may undergo an early-stage pyramidalization for the transition from the bright S_1-state to the dark, reactive S_2-state with more electron rich arenes requiring less pyramidalization. However, Yang *et al.* showed by nonadiabatic molecular dynamics simulations that the reactive DBI pathways of hemithioindigo are defined by conical intersections dominated by dihedral torsion with a rather weak degree of pyramidalization.[50]
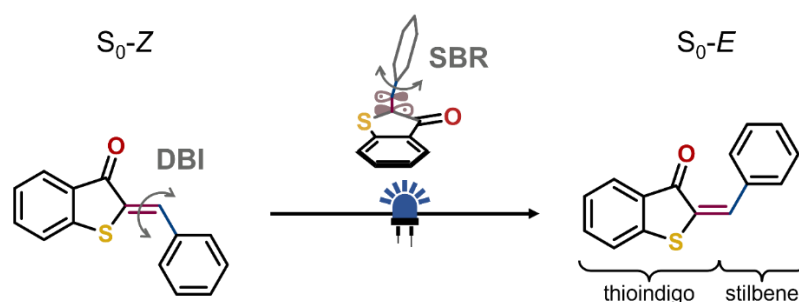
Scheme 1. Z and E isomers of hemithioindigo (HTI) resulting from photoinduced torsion of the thioindigo- and the stilbene fragments around the -C=C- bond. Apart from the illustrated double bond isomerization (DBI), the photoswitch may also undergo single bond rotation (SBR) via flipping of the benzene moiety around the =C-C- bond (center).

As can be seen by the multitude of HTI applications mentioned above, suitable functionalization of these molecular photoswitches is key for developing more complex and capable functions in the future. For a truly rational design of such advanced capabilities, in-depth mechanistic understanding of the photochemistry of HTIs and the effect of the functionalization is required - both at the electronic and the molecular scale. From the perspective of theory, such characterization may be provided by time-dependent density functional theory (TD-DFT) calculations and more sophisticated multireference methods to study the electronic states, whereas molecular dynamics (MD) simulations offer the investigation of atomic motion using classical Newtons dynamics. The key hurdle to MD investigations is however given by the need to appropriately describe the forces and energies of the atomic interactions – both in the electronic ground state and after photoactivation. While the most accurate approach would call for a fully quantum treatment of both electronic and vibrational degrees of motion, the computational costs of such modelling are quite considerable. As a consequence, only models of a few selected degrees of freedom could be subjected to full quantum dynamics simulations at the current state of the art.

Molecular photoswitches including HTI are highly sensitive to the environment and it is of critical importance to understand the details of solvent effects or HTI embedding in molecular assemblies such as self-assembled monolayers.[55,56] We therefore advocate for explicit solvent models and extended statistical sampling – which implies 10,000s of atoms sized simulation systems and 100 ns scale dynamics runs, respectively. This calls for computationally efficient approaches that largely replace quantum mechanical (QM) calculations by molecular mechanics (MM). This may be accomplished by multi-state force-fields to specifically describe Born-Oppenheimer potential energy profiles at a given electronic state. The latter are routinely available for the ground state,

however for photoswitches we also need specific force-fields for describing the modification of the atomic forces upon electronic excitation. As a minimum requirement, at least the most relevant excited state, typically the adiabatic S_1, needs to be mimicked by a tailor-made MM interaction potential.

To model the photoinduced excitation process, multi-state force-fields may be connected to surface-hopping approaches that implement transition probabilities based on QM calculations.[57,58] In a QM/MM fashion, the underlying QM system is often limited to the photoswitch molecule, whereas embedding effects (solvent, local aggregates etc.) are efficiently described by MM approaches. On the other hand, once the electronic state has changed we may investigate photoswitch relaxation from straight-forward MD simulation using the $S_0/S_1/...$ -specific MM force-fields.[59] This enables the investigation of geometry changes from Newtons dynamics rather than imposing minimum energy pathways. Moreover, the interplay with the embedding environment is assessed from explicit atomic movement of the nearby molecules.

In what follows, we develop S_0/S_1 -specific MM force-fields for the parent HTI and demonstrate the analysis of solvent effects from detailed MD simulations. Apart from the underlying energetics, a particular focus is dedicated to statistical sampling. This enables also assessing entropic and kinetic effects – which we argue are becoming of increasing relevance with the increasing complexity encountered in photoswitches and their derived molecular machines in particular.

Models and Methods:

Unless otherwise noted, all quantum chemical calculations were carried out using Kohn-Sham density functional theory (DFT) as implemented in the ORCA 5.0.4 quantum chemistry software package[60,61] using the B3LYP[62] exchange-correlation functional in combination with the def2-TZVP basis set[63] and the def2/J auxiliary basis.[64] Dispersion was treated by Grimme's D3 dispersion correction[65] including the Becke-Johnson damping function.[66] Acceleration of the calculations was achieved by applying resolution of identity approximation[67] and chain of spheres exchange.[68] To assess the nature of stationary points, the vibrational frequencies of all optimized geometries were calculated by applying the harmonic oscillator approximation. From this, we ensure the absence of imaginary frequencies for identifying minimum energy configurations on the potential energy surface.

All molecular mechanics force field parameters – except for the new terms – were derived from the General AMBER Force Field (GAFF) 2.2.20 suite,[69] as released with the Amber22 software package.[70] Atomic partial charges were obtained by the restricted electrostatic potential (RESP) method fit.[71] The corresponding electrostatic potential was obtained from the DFT optimized structures using a Hartree-Fock calculation on a 6-31G** basis[72–76] as implemented in Gaussian16.[77] Consequently, the RESP charges were generated using Antechamber.[78]

Molecular dynamics simulations were performed using the Large-scale Atomic/Molecular Massively Parallel Simulator (LAMMPS)[79] using a time step of 1.0 fs. Temperature and pressure were controlled by applying the Nosé-Hoover thermostat-barostat algorithm as implemented in LAMMPS using relaxation constants of 0.1 ps and 1.0 ps for temperature and pressure, respectively. Non-bonded short-range

interactions were cut off at a distance delimiter of 12 Å. To account for long-range Coulomb interactions, the particle-particle particle-mesh Ewald approach was utilized. All NVT simulations were performed at 300 K and all NpT simulations at 300 K and a pressure of 1 atm, respectively.

All molecular dynamics simulations in explicit solvation boxes were preceded by 10 ns of NpT equilibration of the bulk solvent, followed by additional 10 ns runs after insertion of the HTI molecule. Apart from the gas phase, photoswitching was investigated in n-hexane and dimethyl sulfoxide (DMSO) using cubic, 3D-periodic simulation models of 508 and 991 solvent molecules, respectively. For each isomer, Z and E, parallel systems were prepared and propagated for 50 ns in the NpT ensemble to provide volume relaxation. While 2 ns were found necessary for equilibration, the occurrence profiles of the torsion angle in the different states were derived from the remaining sketches of 48 ns. We then fixed the box volume to the mean volume of the NpT equilibration run and performed an additional NVT run of 50 ns, taking snapshots at every 10 ps. This provided 5,000 structures referring to the (solvated) Z- and E-structures in the S_0 state that were used as the starting structures for investigating photoexcitation to S_1. The trajectories of the actual switching events were propagated in the NVE ensemble, using an initial 20 ps run in the S_1 state and then instantaneously switching back to the S_0-FF to produce additional 5 ps NVE runs that describe the $S_1 \rightarrow S_0$ switching, respectively.

Based on parallel series of 2×5,000 switching trajectories created in this manner, the probability of ($S_0 \rightarrow S_1 \rightarrow S_0$) relaxation to the S_0-E state was scrutinized by committor analyses referring to the atomic coordinates of the model systems at the moment when switching the force field according to the $S_1 \rightarrow S_0$ transition. For each of the geometric

features investigated, occurrence profiles were sampled using 20 equidistant bins within the observed minimum and maximum values, respectively. On the basis of this discrimination, conditional committor probabilities are sampled and subjected to a sigmoid fit using a logistic regression classifier as implemented in Scikit-learn version 1.5.0.[80] Prior to model training, the feature sets were recentered and rescaled using the StandardScaler from the Scikit-learn library. No penalty was added to the logistic regression model.

The solvent distribution was analyzed using a voxel grid of 48 x 48 x 48 with voxel size of $(0.5 \text{ Å})^3$ to sample the density of DMSO/n-hexane molecules around the HTI solute. For the sampling of occurrence statistics, each configuration was aligned according to the HTI position and orientation as defined by the C^{13}, C^{14} and S^{15} atoms (see fig.1 for notations), respectively.

Results and Discussion:

Molecular mechanics models of HTI torsion in S_0 and S_1/T_1 states

The torsion profile of the core HTI molecule features two (local) energetic minima in each, the S_0 and S_1 states, respectively (figure 1). Using unrestrained geometry optimization from DFT calculations, we prepared reference models of these key structures. The underlying S_0/S_1 type minimum energy structures of HTI are used for computing the atomic partial charges of the MM models.
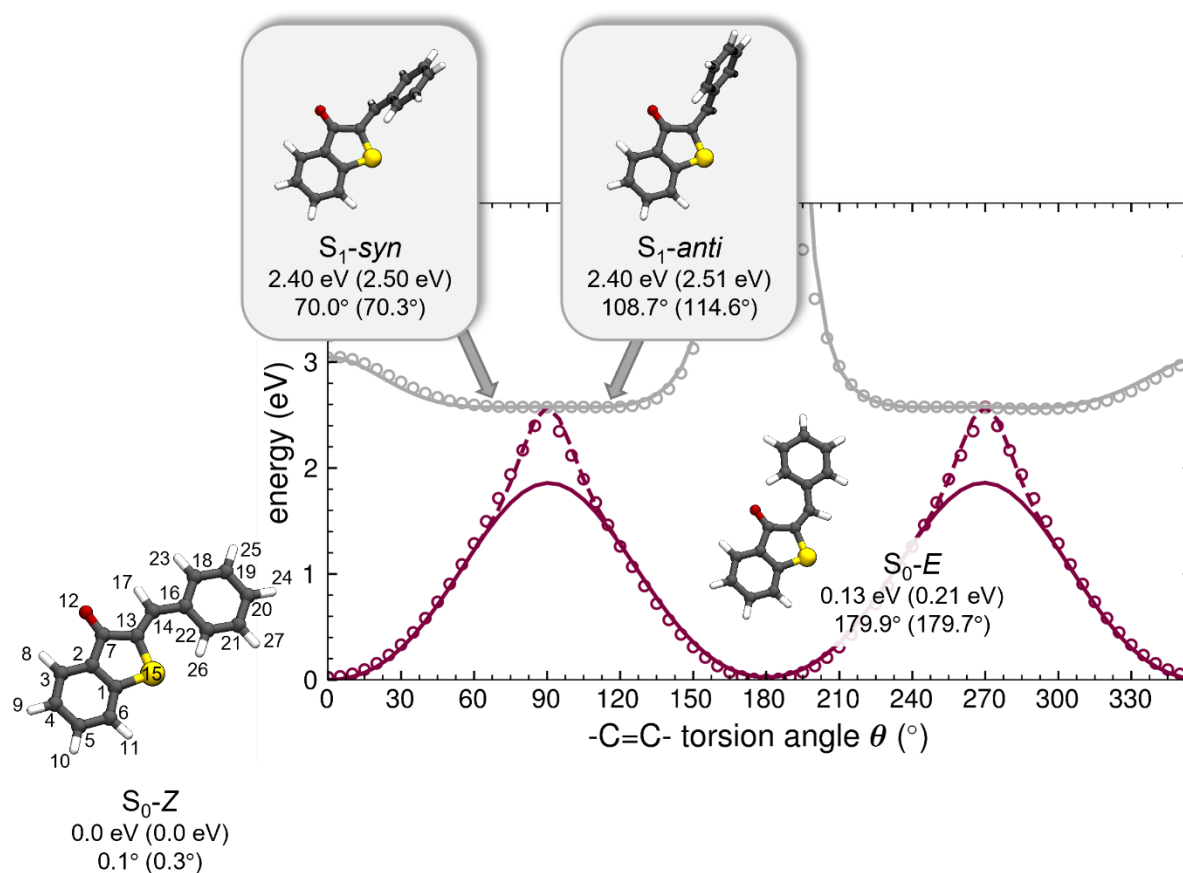

Figure 1. Locally stable configurations of HTI (minimum energy arrangements shown for the MM models; values in brackets refer to the DFT reference) and energy profiles for the torsional rotation around the central -C=C- double bond as computed for the S_0 (red) and the (T1-derrived) S_1 (grey) states, respectively. The reference DFT calculations (B3LYP-D3(BJ) / def2-TZVP) are shown by dots, whereas the solid/dashed curves refer to the corresponding MM models, respectively.

Starting from the DFT-relaxed S_0-*E* and S_1-*syn* structures, rigid scans of the -C=C-torsion were performed in parallel runs. While such rigid scans are particularly useful for parameterization of the torsion potentials without interference from lateral movements, we suggest the fully relaxed minimum energy configurations S_0–*Z/E* and S_1–*syn/anti* for benchmarking our MM models.

For the electronic ground state S_0, we find that the standard GAFF model only partially reproduces the energy profile as observed from the QM reference calculation. Hence, we re-fitted the –C=C- torsion potentials originally provided as a sum of cosine terms

$$V_{\mathrm{dihedral}}(\theta) = \sum_i k_i\big[1 + \cos\big(n_i\theta - \theta_{i,0}\big)\big] \tag{1}$$

to improve the force constants k_i and phase shifts $\theta_{i,0}$ as denoted in the supplementary information S1, respectively. Moreover, we introduce a correction term to better reproduce the energy barriers by adding:

$$V_{\mathrm{corr}}(\theta) = k_{\mathrm{corr}} \cdot \cos\left(\theta - \frac{\pi}{2}\right)^{2\cdot n_{\mathrm{corr}}} + E_{\mathrm{corr}}^0 \tag{2}$$

where n_{corr} = 19, k_{corr} = 16.5 kcal/mol and $E_{\mathrm{corr}}^0 = -11.75$ kcal/mol, respectively, was found to provide the desired local nature of refining the energy profile near the torsion barriers.

In turn, electronic excitation manifests in changes in the atomic partial charges and the -C=C- torsion potential as a minimum to finding appropriate MM models. While the actually relevant electronic excitation describing photoswitching refers to the adiabatic S_1 state, a simple numerical trick in the DFT calculations is to first characterize the

more stable T_1 state, which corresponds to the lowest non-relativistic energy eigenstate for a total electron spin of 1, followed by subtracting two times the exchange potentials to yield the S_1 energy. On this basis, numerically robust scans of torsional degrees of freedom and valence angles can be performed to parametrize the MM potentials. [59]

The underlying rigid scans require sterically reasonable starting points – which we picked from the DFT-relaxed S_0-*E* and S_1-*syn* (actually T_1-*syn*) structures, respectively. To this end, the explicit atomic structures used for computing the S_1-state torsion profile do not fully match those of the S_0-state based scan, albeit featuring the same torsion angle θ. In fig. 1, the conical intersection is prepared by matching the MM-based S_1 profile to the MM-based S_0 torsion barrier. In TD-DFT, the conical intersection prevents numerical assessment of S_1 energies for the HTI structures near $\theta = 90°$ as already demonstrated by Plötner and Dreuw.[48] To assess the energy shift between T_1 and S_1, we instead used the S_0-*Z* and S_0-*E* configurations at 90°, which showed offsets of $2 \cdot \Delta E_{exchange} = 0.80$ and 0.74 eV, respectively. Our excited-state MM models fitted to the T_1-based DFT energies of the torsion profile, are thus suggested to use a constant shift of 0.77±0.03 eV to mimic the corresponding S_1-states.

Fitting MM models to the DFT-based references required careful inspection of a series of interaction terms. To this end, accurate energy profiles for the S_0-state are readily obtained from adding the correction term described in eq. (2) to the newly parametrized GAFF-type torsion potentials described in eq. (1) and by new Lennard-Jones parameters for the pairwise interaction between H-atoms 23/26 and the oxygen/sulfur species, respectively. In turn, the MM model describing the T_1/S_1-states involves a set of new atomic partial charges, and specific GAFF parameters as denoted in the

supplementary information S1. The latter includes re-parameterization of the GAFF models for the covalent bonding potentials of central bonds, along with their valence and torsion potentials.

The numerical robustness of the MM potentials now allows the (approximate) assessment of the S_1-energy near the diabatic crossing. Indeed, the HTI structure of the S_0-based torsion profile experiences a barrier of 2.57 eV at $\theta=90°$ - whilst the S_1-type MM model applied for the *same* atomic configuration predicts 2.65 eV, respectively. To this end, application of the MM models to the S_0-related structures actually predicts an avoided crossing scenario, albeit at an energy difference of only 0.08 eV.

MD simulation of HTI in S_0 and S_1 states: vapor, hexane and DMSO

Before looking into the actual $Z{\rightarrow}E$ isomerization process, we characterized the underlying local energy configurations by separate MD simulations in the NpT ensemble (50 ns at T=300K). Figure 2 shows the occurrence profiles $h(\theta)$ of the -C=C-torsion angle θ, for i) HTI in the gas phase, solvation in ii) n-hexane and iii) DMSO, both at ambient conditions, respectively. As a consequence of the large torsion barrier in the S_0-state, two separate profiles were derived for the *Z*- and *E*- conformers, respectively, using parallel MD runs. On this basis, the average energy difference in S_0-*Z* and S_0-*E* conformers was found as 0.13, 0.11 and 0.14 eV in the vapor, hexane and DMSO studies, respectively (see supplementary information S2, figure S2.1). To this end, for all solvent environment studies, the thermodynamically stable S_0-state is

given by the S_0-Z conformer, and Boltzmann statistics at 300K would predict at most 1.4 % population of the S_0-E conformer.

In view of the ~2 eV energy barrier separating the Z- and E- conformers in the S_0-state, such thermodynamic considerations only apply to rather long-termed relaxation. In turn, short-term HTI relaxation upon photoexcitation and electronic decay occurs on the ps scale and will thus critically depend on the HTI arrangements in the S_1 state. To highlight the role of the solvent environment for the S_0-$Z \rightarrow S_1 \rightarrow S_0$-$E$ isomerization, we therefore also sampled the occurrence profiles $h(\theta)$ of the -C=C- torsion angle in the S_1 state. Each of the three occurrence profiles is normalized to 1 and, at this stage, no transitions between the three states are considered. As a consequence, the solvent effect is characterized for each HTI conformer individually, allowing full relaxation of all solvent degrees of freedom. The occurrence profiles shown in fig. 2 thus reflect the thermodynamics of HTI vibrations and their interplay with the different electrostatics and van-der-Waals interactions.
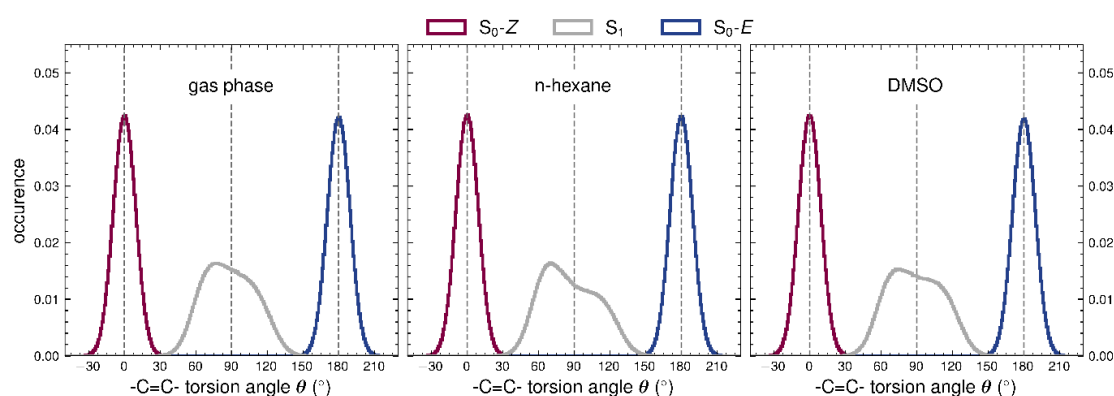

Figure 2. Occurrence profiles of the -C=C- torsion angle of HTI in vacuum (left), n-hexane (center), and DMSO (right). While well-defined peaks are observed for the solvation of the S_0-Z and -E states, we find significant changes in the statistics collected for the S_1-*syn/anti* conformers. Steric hindering and van-der-Waals interactions in hexane promotes S_1-*syn* type arrangements, whilst electrostatics and hydrogen bonding lower the relative energy of the S_1-*anti* conformer in DMSO.

For each of the solvent scenarios i)-iii), the average torsion angle of HTI in the S_1-state is near 90° - albeit at rather asymmetric, bi-modal distributions. Based on the MM potentials, we can rationalize this finding by means of contrasting individual contributions to the overall interplay of interaction forces. Since the mathematical term describing the torsion potential in the S_1-state is symmetric around 90°, any asymmetry must originate from the intramolecular pairwise interactions – e.g. Lennard-Jones and Coulombic potentials – specifically the interaction of the stilbene moiety and H[17] with the carbonyl group and the sulfur atom, respectively (see also fig.1). Hexane amplifies the asymmetry in favor of smaller -C=C- torsion angles (fig. 2, center). In turn, DMSO induces an opposite effect, stabilizing larger torsion angles (fig.2, right). This observation is attributed to explicit solvent-solute interactions, which we argue is mainly of van-der-Waals nature for hexane, whereas the different trend observed in DMSO should result from over-compensation of van-der-Waals forces by Coulomb interactions.

MD simulation of the photoisomerization process

Based on the relaxed S_0-*Z* and S_0-*E* configurations (in vapor, hexane and DMSO) as discussed above, we now look into the photoexcitation to S_1 by means of MD simulation. For this, 2×5000 randomly depicted snapshots were taken from NVT runs for each isomer, subjected to instantaneous switching to the S_1-MM model, and propagation from MD simulations. Relaxation in the S_1 state was monitored in the NVE ensemble to avoid artificial damping of the kinetics by the thermostat algorithm.

Sampling averages from the (each) 5000 pathways collected for the S_0-Z and S_0-E starting points, respectively, we produced time-dependent profiles of the -C=C- torsion angle (fig.3, see also supplementary information S3.1). The different relaxation dynamics are best seen from contrasting S_0-$Z/E \rightarrow S_1$ in vapor to HTI photoswitching in solution, respectively. In the former, 0/180° $\rightarrow$ 90° deformation of the -C=C- torsion angle is observed on the fs scale, however leading to strong vibrations of the entire HTI molecule – and thus re-visiting the Z/E type configurations. In turn, after energy dissipation from the torsion degree of freedom to molecular vibration, we find convergence to the S_1 state within about 10 ps. On the other hand, in solution the torsional motion is slowed by nearby solvent molecules. This damps HTI vibrations significantly and convergence to the equilibrium S_1 state is found at the 5 and 15 ps scale in hexane and DMSO, respectively. Statistics of the vertical energy difference between the S_0- and the S_1-state are reported in the supplementary information S3, whereas the electronic decay from S_1-states is discussed in the following.
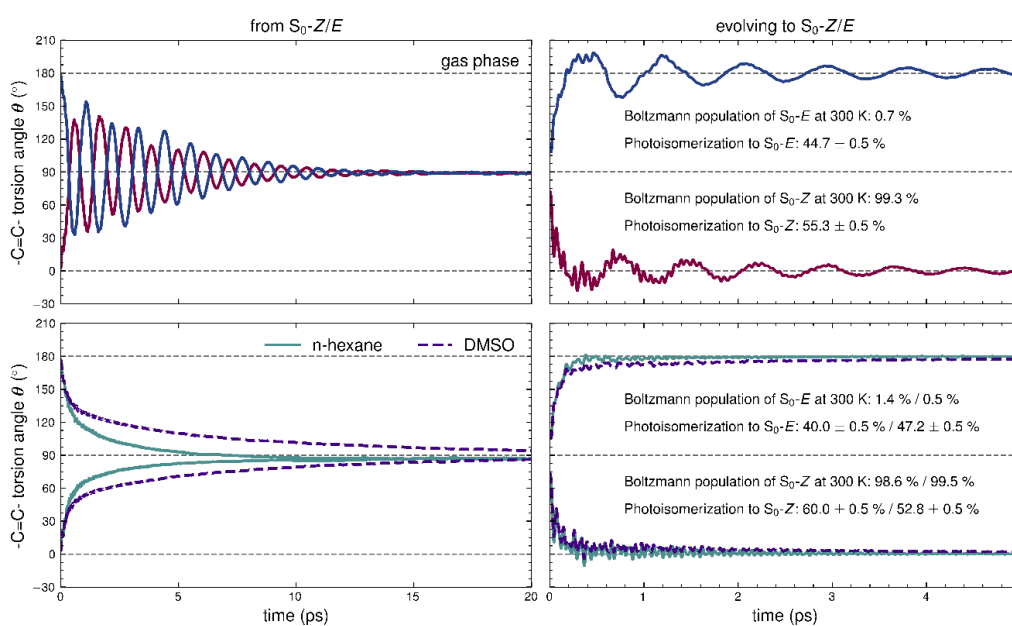

Figure 3. Time-dependent profiles of the -C=C- torsion angle upon S_0-$Z/E \rightarrow S_1$ excitation (left row) and, after 20 ps propagation in S_1, electronic decay back to the ground state (right). Averages collected from

5,000 individual trajectories starting in S_0-Z and 5,000 trajectories starting in S_0-E, respectively, are shown for HTI in vacuum (upper panel) and in n-hexane / DMSO (lower panel). From the overall statistics of the 10,000 pathways mimicking the electronic decay to the ground state, we find the $S_1 \rightarrow S_0$-Z transition to be preferred, namely 55.3 % of the runs performed in vapor evolved to the S_0-Z isomer. In turn, the role of the solvent is reflected by the change in $S_1 \rightarrow S_0$-Z committor probability - which increases to 60.0 % in hexane, whereas a reduction to 52.8% is observed in DMSO, respectively.

From comparing the evolution of photoswitching pathways starting from S_0-Z and S_0-E, we argue that upon 20 ps propagation in the S_1 state, our MD simulations converged to S_1 type configurations. Using the endpoints of these 2×5000 trajectories, we switched our MM model back to the S_0 state to mimic the electronic decay to the ground state. In all solvent scenarios, we find the HTI molecules to lock into either S_0-Z or S_0-E configurations within only a few picoseconds of NVE simulation runs (fig.3). While evolution to the S_0-Z state is preferred over all solvent scenarios, the observed Z/E ratio after completing the photoswitching cycle differs significantly. Indeed, the probability of finding S_0-Z conformers (which was found as 55.3 % for the $S_1 \rightarrow S_0$-Z transitions in vapor) increases to 60.0 % in n-hexane whereas a reduction to 52.8 % is observed in the DMSO case.

The $S_1 \rightarrow S_0$-Z transition probabilities are in stark contrast to the ratio of S_0-Z and S_0-E conformers one would expect from simple Boltzmann statistics based on the corresponding averages in energy. Thus, despite providing generous relaxation time (20 ps) in the S_1 state, we still find a kinetic biasing of the Z-E photoisomerization. It is intuitive to expect the momentous -C=C- torsion angle to play a key role for the fate of the HTI molecules upon electronic decay from the S_1 state. In turn, the identification of further descriptors for evolution to Z- or E-conformers is much less obvious. For this reason, we performed a committor analysis based on the manifold of MD pathways

collected for the $S_1 \rightarrow S_0$ transition runs. To this end, the probability of HTI relaxation to the *E*-isomer p($S_1 \rightarrow S_0$-*E*) is assumed as the reaction coordinate. While mathematically exact, it however provides little help for our actual understanding of the underlying mechanisms. This motivates the formulation of structural descriptors of which we created a small series of candidates from intuition.

To benchmark the suitability of a given descriptor *x* as a trigger for enhancing/diminishing *Z-E* isomerization by photoexcitation, we elucidate its performance in predicting the 'mathematical reaction coordinate' p($S_1 \rightarrow S_0$-*E*,x). The latter refers to the above-described statistics of p($S_1 \rightarrow S_0$-*E*) - which was devised as a function of *x,* that is the value of the given descriptor at the instant of the electronic decay $S_1 \rightarrow S_0$ (implemented by switching of the MM models). This target function is approximated by a sigmoid-type fit function p(*x*) according to:

$$\mathrm{p}(S_1 \rightarrow S_0 - E, x) \approx \mathrm{p}(x) = \left(1 + A \cdot e^{-\omega \frac{x - \langle x \rangle}{rmsd(x)}} \right)^{-1} \tag{3}$$

Inspired by the fitting of logistic regression classifiers, two parameters *A* and ω are used to best approximate our target function, namely p($S_1 \rightarrow S_0$-*E*,x) as sampled from the corresponding occurrences observed from our MD runs. To this end, parameter *A* controls $\mathrm{p}(x = \langle x \rangle)$ – which is reflected by the overall average of p($S_1 \rightarrow S_0$-*E*). In turn, the parameter ω indicates how sharply the sigmoid shape of p(*x*) depends on the actual value *x* of the descriptor. This allows interpreting ω in terms of the suitability of a given descriptor model. For example, a poorly chosen descriptor that does not correlate at all with p($S_1 \rightarrow S_0$-*E*,x) will essentially provide random numbers as inputs to p(*x*). The corresponding fit will thus show ω = 0 and p($S_1 \rightarrow S_0$-*E*,x) = p($S_1 \rightarrow S_0$-*E*) is a constant. On the other hand, the larger |ω|, the more sensitive is the fitted function p(*x*) and the

better will be the prediction of the target $p(S_1 \rightarrow S_0\text{-}E,x)$. We therefore suggest $|\omega|$ as an indicator for how strong a given descriptor triggers the committor probability.

For HTI switching in vacuum, only the DBI torsion angle $\theta_{\text{-}C=C\text{-}}$ could be identified as a significant descriptor for triggering relaxation to $S_0\text{-}Z$ versus $S_0\text{-}E$ from the S_1-state. In fig. 4, this is indicated by a well-defined sigmoid shape of the fitted function $p(x)$ for predicting the committor probability $p(S_1 \rightarrow S_0\text{-}E,x)$. For comparison, we also show the fitting of eq. 3 in case of using the SBR torsion angle $\theta_{=C\text{-}C\text{-}}$ as a putative descriptor. In this case, we indeed find $\omega=0$ and a rather indifferent approximation of $p(S_1 \rightarrow S_0\text{-}E,x)$ = constant.
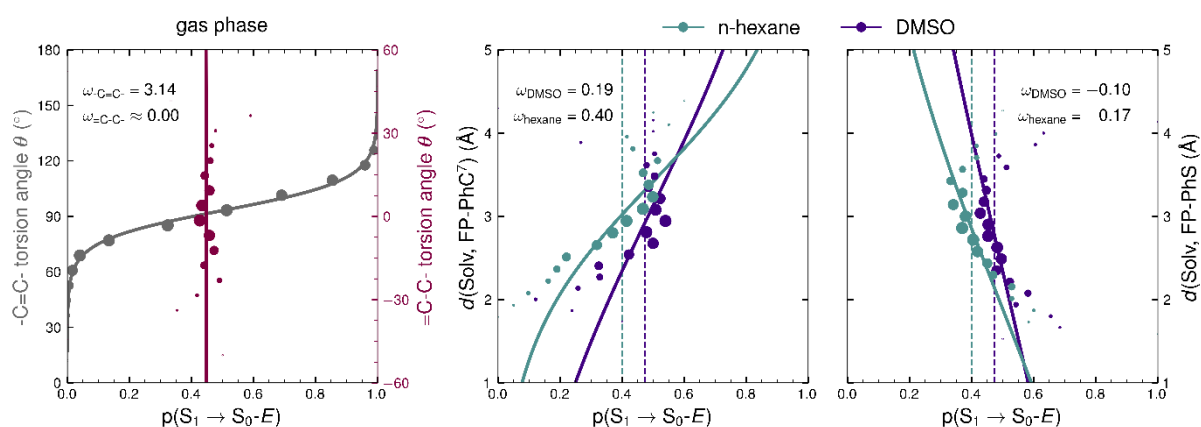

Figure 4. Committor analyses for the photoswitching of HTI in gas phase (left) and in hexane (center) and DMSO (right) solution. The dots refer to the statistics collected for the probability of reaching the S_0-E configuration - devised as a function of possible descriptor variables x at the moment of switching from S_1 to S_0. The dot sizes are proportional to the number of trajectories committing to the respective data point. The solid curves refer to the fitting of sigmoid type functions (eq.3) – which suitability for predicting the triggering of relaxation to S_0-E is quantified by $|\omega|$. The factors A amount to 1.59, 1.23, 1.52, 1.50, 1.12, and 1.12 for the cases of $\theta_{\text{-}C=C\text{-}}$, $\theta_{=C\text{-}C\text{-}}$, d(hexane, FP-PhC[7]), d(hexane, FP-PhS), d(DMSO, FP-PhC[7]), d(DMSO, FP-PhS), respectively.

 ORCID: https://orcid.org/0000-0002-5968-2216

A more subtle picture is however observed for HTI photoswitching in solution. While the $\theta_{\text{-C=C-}}$ angle is still of central importance for *Z-E* isomerization, we identified two solvent coordinates as additional descriptors for predicting our committor analyses. Indeed, to study the influence of explicit solvent molecules on the photoswitching, we defined focal points (FPs) representing key features of the HTI geometry and sampled their distance to nearby solvent atoms. For this, we computed the center-of-geometry of the phenyl ring (Ph) and suggested its geometric center between the C^7 / S atoms of HTI as FP-PhC^7 / FP-PhS sites to elucidate the coordination of nearby solvent molecules (fig.5).
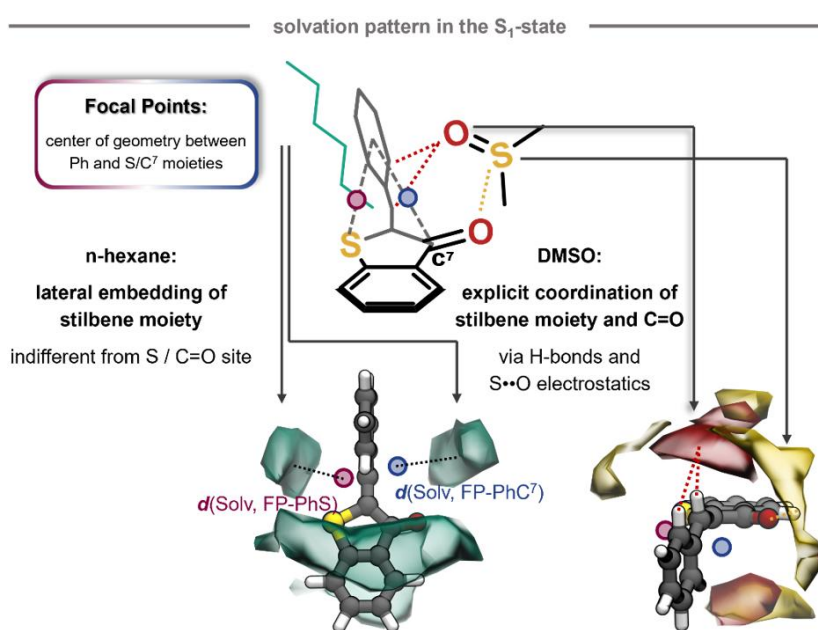

Figure 5. Top: Schematic representation of HTI in the S_1-state illustrating the focal points (FP-PhS, FP-PhC^7) defined as the geometric centers between the HTI phenyl ring and the S/C^7 moieties, respectively. Lower panel: occurrence profiles of nearest neighbor solvent atoms to FP-PhS and FP-PhC^7, showing nearest neighbor C_{hexane} (iso: 0.05 Å^{-3}), O_{DMSO} (iso: 0.022 Å^{-3}) and S_{DMSO} (iso: 0.022 Å^{-3}) atoms in green, red and yellow color, respectively.[81] Solvation in hexane features lateral embedding of the stilbene fragment with roughly equal occurrence of solvent molecules next to either of the focal points. In turn, we find sharply defined coordination by DMSO via electrostatic interactions with the carbonyl oxygen and H-bonds to the stilbene moiety of HTI.

The nearest-neighbor distance of solvent species and the FP-PhC[7] / FP-PhS sites essentially describes whether a solvent molecule blocks HTI flipping to S_0-E or S_0-Z, respectively. In the case of HTI solvation in hexane, we find such blocking as a largely kinetic effect. In average, lateral coordination of the stilbene moiety shows no favoring with regard to association next to FP-PhC[7] or FP-PhS – as the underlying van-der-Waals interactions are rather indifferent. Nevertheless, the momentous solvent arrangement at the instant of switching to the S_0-state is more decisive, as solvent molecules close to FP-PhC[7] tend to block HTI torsion towards the S_0-E geometry (fig.4, center). Likewise, the closer solvent species are to FP-PhS the more likely the solvent may block HTI flipping to the S_0-Z geometry (fig.4, right).

To discriminate these solvation effects, we suggest four prototype cases depending on the minimum solvent distances to FP-PhC[7] and FP-PhS, respectively. For this, delimiters of 2.5 Å regarding the nearest solvent atom distances d(solv, FP-PhC[7]) and d(solv, FP-PhS) were found suitable for a clear-cut discrimination. As case 1 we refer to the situation d(solv, FP-PhC[7]) < 2.5 Å and d(solv, FP-PhS) > 2.5 Å. From a purely steric viewpoint, case 1 implies the presence of a solvent molecule that stacks with immediate HTI rotation to S_0-E, whereas no blocking of $S_1 \rightarrow S_0$-Z is expected. In turn, case 2 is considered as the inverse of case 1, namely a solvent molecule that hinders $S_1 \rightarrow S_0$-Z rotation whilst no blocking to S_0-E is expected. Finally, cases 3 and 4 are defined as fully blocking as compared to fully allowing HTI rotation (to either S_0-E or S_0-Z), respectively. We compared the conditional committor probabilities $p(S_1 \rightarrow S_0$-E,case 1-4) of all trajectories for the different cases (table 1) to the overall averages (see also fig. 3).

Among the prototype classes, case 4 – that is, no close contact to either FP-PhC[7] nor FP-PhS – refers to the most frequently observed solvent arrangement. The corresponding committor probability of $p(S_1 \rightarrow S_0\text{-}E)$ = 40.5 (hexane) and 48.4 % (DMSO), respectively, may be considered as reference points when contrasting the effect of closer solvent contacts. Indeed, cases 1 and 2 show the decline/increase of $p(S_1 \rightarrow S_0\text{-}E)$ by -23.5 / +10.6 % in hexane and -18.0 / +5.0 % in DMSO, respectively. We thus argue that steric hindering is of particular importance for $S_1 \rightarrow S_0\text{-}E$ rotation – which may be related to the space demand of the carbonyl group of the HTI molecule. This is also reflected by the statistics collected for case 3, i.e. for lateral solvent contacts close to both FP-PhC[7] and FP-PhS sites, respectively. In such case, we still find preferential relaxation towards $S_1 \rightarrow S_0\text{-}Z$ – suggesting that steric hindering is most critical for stilbene rotation towards the carbonyl group (as needed for reaching the $S_0\text{-}E$ configuration).

	$p(S_1 \rightarrow S_0\text{-}E)$ (%)	
	n-hexane (N_{traj})	DMSO (N_{traj})
Case 1	17.0 (852)	30.4 (1,107)
Case 2	50.6 (1,812)	53.4 (2,278)
Case 3	21.1 (161)	37.0 (284)
Case 4	40.5 (7,175)	48.4 (6,331)
All	40.0 (10,000)	47.2 (10,000)

Table 1. Conditional committor probability of reaching the $S_0\text{-}E$ isomer upon electronic decay from S_1. The values in brackets refer to the total counts collected from a total of 10,000 photoswitching trajectories.

While the discussed steric effect triggered by the momentous solvent environment applies to both hexane and DMSO, the case-dependence of the $p(S_1 \rightarrow S_0$-$E)$ committor probabilities is much more pronounced in hexane. This is somewhat surprising as we found DMSO to coordinate to FP-PhC[7] via H(phenyl)••O(DMSO) / H(vinyl)••O(DMSO) hydrogen bonding and S(DMSO)••O(carbonyl) electrostatics, thus favoring DMSO association next to the carbonyl moiety of HTI (fig. 5).

To resolve this apparent contradiction, we sampled the nearest-neighbor solvent arrangement a) at the moment of the electronic transition $S_1 \rightarrow S_0$ and b) after 200 fs relaxation dynamics in the S_0-state (fig. 6). For HTI solvation in hexane, such before/after analysis of nearby solvent atom distribution clearly shows the steric hindering effect: solvent atoms close to FP-PhC[7] are shoved aside during the hinge motion of the phenyl ring while the solvent on the opposing side of the stilbene moiety is following this motion. In stark contrast to this solvation mechanism, the coordinating DMSO molecule moves concertedly with the stilbene moiety to keep the hydrogen-bonding pattern upright. Hence, the lower extend of steric hindrance experienced for HTI switching in DMSO may be related to a less dense solvation of the phenyl ring (fig. 5) and the concerted rotation motion of DMSO coordinating the stilbene moiety (fig. 6).
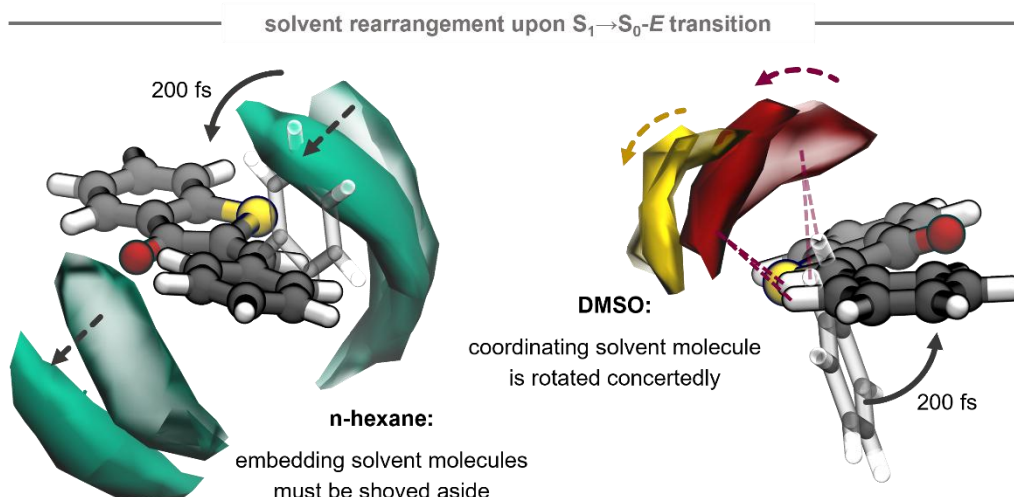
Figure 6. Isosurface plots of the 3-dimensional occurrence profile of solvent atoms. Left: C_{hexane} (iso: 0.05 $Å^{-3}$). Right: O_{DMSO} (iso: 0.022 $Å^{-3}$, red), S_{DMSO} (iso: 0.022 $Å^{-3}$, yellow). Transparent surfaces correspond to the solvent distribution at the $S_1 \rightarrow S_0$-E transition, opaque surfaces correspond to the solvent distribution 200 fs after. The plots were generated from all structures resulting in the formation of the E-isomer. For clarification, only the most important solvent density isosurfaces are shown.

Single bond rotation

In parallel to the photoinduced double bond isomerization described above, we also studied possible rotation of the stilbene moiety around the =C-C- single bond from the series of $S_0 \rightarrow S_1 \rightarrow S_0$ transition trajectories. While SBR is readily observed in hemithioindigo chromophores with asymmetrically substituted phenyl rings[43,53], it cannot be resolved experimentally for the unsubstituted HTI due to the chemically indistinguishable photoproducts. Nevertheless, our molecular models allow for indexing the individual atoms to provide such discrimination. As a consequence, we may study SBR for perfectly symmetric units – and thus elucidate the photoreaction in absence of thermodynamic favoring of either conformer. This allows studying kinetic

effects in a stand-alone manner, unbiased from energetic effects that would result from asymmetric substituents.

From the series of 10,000 $S_1 \rightarrow S_0$ switching simulations in n-hexane and DMSO, we find only 2.4 % and 2.5 % to show SBR , respectively. Notably, each of the switching events implies a gain in kinetic energy of the HTI molecules, which of course firstly affects the dynamics of the $\theta_{-C=C-}$ torsion angle – but is also reflected in the fluctuations of the $\theta_{=C-C-}$ torsion angle. However, effective SBR is only observed in case of $S_1 \rightarrow S_0$ transition at momentous arrangements exhibiting $\theta_{-C=C-}$ near 90°, whereas clear triggering of DBI by $\theta_{-C=C-} > 90°$, or likewise clear disfavoring of DBI by $\theta_{-C=C-} < 90°$ tends to diminish the chances for SBR, respectively. In fig. 7, this is illustrated by means of two representative trajectories. In addition, statistical analyses of the manifold of pathways are reported in supplementary information S4.
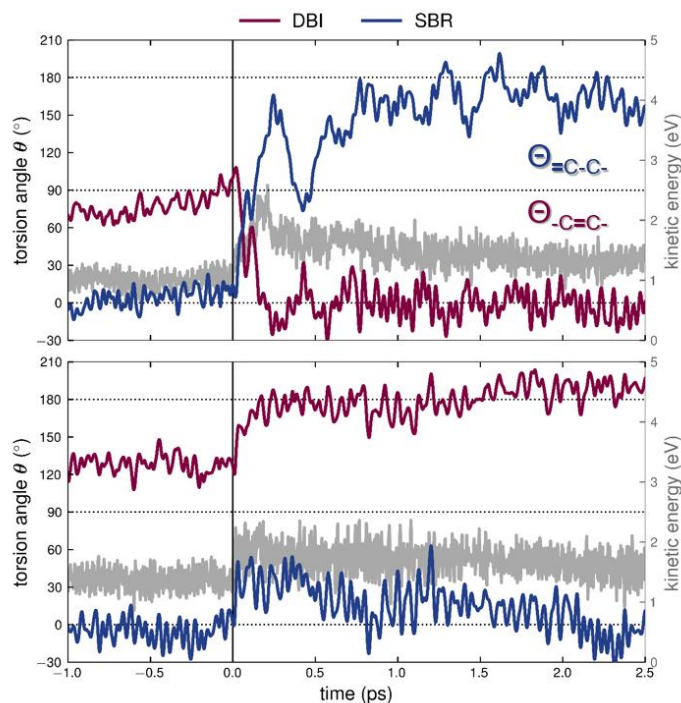

Figure 7. Exemplary trajectories showing HTI relaxation in n-hexane upon $S_1 \rightarrow S_0$ transition (at time t=0). The switching firstly affects the $\theta_{-C=C-}$ torsion potential and induces ~1 eV changes in kinetic energy. While the latter is finally dissipated to solvent motions, significant enhancement of HTI vibrations is

observed during the first 0.5 -1 ps after the electronic decay. In 2.4 % of our relaxation trajectories, we find SBR (top), whereas the majority of pathways reflect increase in the amplitude of $\theta_{-C=C-}$ torsion angle vibrations without SBR (bottom).

Apart from the overall amount of kinetic energy gained from $S_1 \rightarrow S_0$ switching in the molecular mechanics models – which is indeed largest for configurations with $\theta_{-C=C-} = 90°$ – the chance of triggering SBR surely depends on the way that the excess kinetic energy is being dissipated. In solution, such dissipation involves both the HTI and nearby solvent species. In turn, HTI switching in the gas phase does permit energy dissipation to other molecules and thus leads to particularly strong enhancement of the vibrations within the HTI itself. Indeed, we found a significantly higher SBR quantum yield of 28.3 % in gas phase. This is in line with a 'hot ground state' picture in which the HTI molecule in vapor retains high kinetic energy after leaving the excited state whilst HTI in solution undergoes energy dissipation with a few picoseconds (see also supplementary information S4).

Conclusion:

In this work, a multi-state molecular mechanics model of the S_0- and S_1-state of HTI was derived from quantum chemical reference calculations. The resulting model offers computationally very efficient MD simulations, whilst retaining a quite reasonable level of accuracy. In turn, our approach enables the study of photoswitching processes in complex environments at appealing statistical quality. Based on 10,000s of dynamical pathways, detailed insights into sub-classes of process routes can be elaborated by means of occurrence statistics and committor analyses.

While in principle enabling much more complex systems, here we demonstrated our approach to assessing the dynamics of HTI photoswitching by the example of a single molecule in vapor and in n-hexane or DMSO solution. From this, it became evident that the solvent effect is not only of thermodynamic nature, but also reflects kinetic aspects. The overall statistics of HTI isomerization via photoswitching (DBI by rotation of the -C=C- dihedral) is mainly determined by steric and electrostatic effects. However, the full picture includes the identification of different mechanisms of solvent re-arrangement dynamics. In turn, SBR rotation (of the =C-C- dihedral) of HTI is triggered by purely kinetic aspects.

We are convinced that our approach offers an exciting perspective for the in-depth understanding of photoswitching and related processes of HTI-based molecules. To one side, QM/MM type extensions offer the assessment of quantum yields for electronic excitation/decay. To the other, the investigation of the relaxation dynamics of a given electronic state relies on efficient molecular mechanics. The transferrable nature of these molecular mechanics models allows describing molecular functionalization without much additional parameterization work (with the assessment of partial charges constituting a minimum). This paves the way to larger scale model

systems, for example of molecular assemblies of HTI-based photoswitches, and their interplay with explicit environment effects such as interface interactions in the future.

Acknowledgements

References:

(1) Koumura, N.; Zijlstra, R. W. J.; van Delden, R. A.; Harada, N.; Feringa, B. L. Light-Driven Monodirectional Molecular Rotor. *Nature* **1999**, *401* (6749), 152–155. https://doi.org/10.1038/43646.

(2) Greb, L.; Lehn, J.-M. Light-Driven Molecular Motors: Imines as Four-Step or Two-Step Unidirectional Rotors. *J. Am. Chem. Soc.* **2014**, *136* (38), 13114–13117. https://doi.org/10.1021/ja506034n.

(3) Guentner, M.; Schildhauer, M.; Thumser, S.; Mayer, P.; Stephenson, D.; Mayer, P. J.; Dube, H. Sunlight-Powered kHz Rotation of a Hemithioindigo-Based Molecular Motor. *Nat. Commun.* **2015**, *6* (1), 8406. https://doi.org/10.1038/ncomms9406.

(4) Chen, K.-Y.; Ivashenko, O.; Carroll, G. T.; Robertus, J.; Kistemaker, J. C. M.; London, G.; Browne, W. R.; Rudolf, P.; Feringa, B. L. Control of Surface Wettability Using Tripodal Light-Activated Molecular Motors. *J. Am. Chem. Soc.* **2014**, *136* (8), 3219–3224. https://doi.org/10.1021/ja412110t.

(5) Groten, J.; Bunte, C.; Rühe, J. Light-Induced Switching of Surfaces at Wetting Transitions through Photoisomerization of Polymer Monolayers. *Langmuir* **2012**, *28* (42), 15038–15046. https://doi.org/10.1021/la302764k.

(6) Ferri, V.; Elbing, M.; Pace, G.; Dickey, M. D.; Zharnikov, M.; Samorì, P.; Mayor, M.; Rampi, M. A. Light-Powered Electrical Switch Based on Cargo-Lifting Azobenzene Monolayers. *Angew. Chem. Int. Ed.* **2008**, *47* (18), 3407–3409. https://doi.org/10.1002/anie.200705339.

(7) Chen, Q.; Wang, Y.; Zhai, J.; Xie, X. Photoswitchable Hemithioindigo Inspired Copper Ion Selective Sensing with Excellent Selectivity and Versatile Operational Modes.

Sens. Actuators B Chem. **2023**, *381*, 133437. https://doi.org/10.1016/j.snb.2023.133437.

(8) Li, J.; Ma, X.; Wang, Y.; Cheng, Y.; Qin, Y.; Zhai, J.; Xie, X. Proton-Coupled Photochromic Hemithioindigo: Toward Photoactivated Chemical Sensing and Imaging. *Anal. Chem.* **2023**, *95* (31), 11664–11671. https://doi.org/10.1021/acs.analchem.3c01504.

(9) Hüll, K.; Morstein, J.; Trauner, D. In Vivo Photopharmacology. *Chem. Rev.* **2018**, *118* (21), 10710–10747. https://doi.org/10.1021/acs.chemrev.8b00037.

(10) Morstein, J.; Trauner, D. New Players in Phototherapy: Photopharmacology and Bio-Integrated Optoelectronics. *Curr. Opin. Chem. Biol.* **2019**, *50*, 145–151. https://doi.org/10.1016/j.cbpa.2019.03.013.

(11) Lerch, M. M.; Hansen, M. J.; van Dam, G. M.; Szymanski, W.; Feringa, B. L. Emerging Targets in Photopharmacology. *Angew. Chem. Int. Ed.* **2016**, *55* (37), 10978–10999. https://doi.org/10.1002/anie.201601931.

(12) Lu, P.; Ahn, D.; Yunis, R.; Delafresnaye, L.; Corrigan, N.; Boyer, C.; Barner-Kowollik, C.; Page, Z. A. Wavelength-Selective Light-Matter Interactions in Polymer Science. *Matter* **2021**, *4* (7), 2172–2229. https://doi.org/10.1016/j.matt.2021.03.021.

(13) Boelke, J.; Hecht, S. Designing Molecular Photoswitches for Soft Materials Applications. *Adv. Opt. Mater.* **2019**, *7* (16), 1900404. https://doi.org/10.1002/adom.201900404.

(14) Nie, H.; Self, J. L.; Kuenstler, A. S.; Hayward, R. C.; Read de Alaniz, J. Multiaddressable Photochromic Architectures: From Molecules to Materials. *Adv. Opt. Mater.* **2019**, *7* (16), 1900224. https://doi.org/10.1002/adom.201900224.

(15) Jia, S.; Sletten, E. M. Spatiotemporal Control of Biology: Synthetic Photochemistry Toolbox with Far-Red and Near-Infrared Light. *ACS Chem. Biol.* **2022**, *17* (12), 3255–3269. https://doi.org/10.1021/acschembio.1c00518.

(16) Konrad, D. B.; Savasci, G.; Allmendinger, L.; Trauner, D.; Ochsenfeld, C.; Ali, A. M. Computational Design and Synthesis of a Deeply Red-Shifted and Bistable Azobenzene. *J. Am. Chem. Soc.* **2020**, *142* (14), 6538–6547. https://doi.org/10.1021/jacs.9b10430.

(17) Velema, W. A.; Szymanski, W.; Feringa, B. L. Photopharmacology: Beyond Proof of Principle. *J. Am. Chem. Soc.* **2014**, *136* (6), 2178–2191. https://doi.org/10.1021/ja413063e.

(18) Petermayer, C.; Dube, H. Indigoid Photoswitches: Visible Light Responsive Molecular Tools. *Acc. Chem. Res.* **2018**, *51* (5), 1153–1163. https://doi.org/10.1021/acs.accounts.7b00638.

(19) Bartelmann, T.; Dube, H. Indigoid Photoswitches. In *Molecular Photoswitches*; John Wiley & Sons, Ltd, 2022; pp 283–302. https://doi.org/10.1002/9783527827626.ch13.

(20) Wiedbrauk, S.; Dube, H. Hemithioindigo—an Emerging Photoswitch. *Tetrahedron Lett.* **2015**, *56* (29), 4266–4274. https://doi.org/10.1016/j.tetlet.2015.05.022.

(21) Ichimura, K.; Seki, T.; Tamaki, T.; Yamaguchi, T. Fatigue-Resistant Photochromic Hemithioindigoes. *Chem. Lett.* **1990**, *19* (9), 1645–1646. https://doi.org/10.1246/cl.1990.1645.

(22) Gerwien, A.; Mayer, P.; Dube, H. Photon-Only Molecular Motor with Reverse Temperature-Dependent Efficiency. *J. Am. Chem. Soc.* **2018**, *140* (48), 16442–16445. https://doi.org/10.1021/jacs.8b10660.

(23) Gerwien, A.; Mayer, P.; Dube, H. Green Light Powered Molecular State Motor Enabling Eight-Shaped Unidirectional Rotation. *Nat. Commun.* **2019**, *10* (1), 4449. https://doi.org/10.1038/s41467-019-12463-4.

(24) Gerwien, A.; Gnannt, F.; Mayer, P.; Dube, H. Photogearing as a Concept for Translation of Precise Motions at the Nanoscale. *Nat. Chem.* **2022**, *14* (6), 670–676. https://doi.org/10.1038/s41557-022-00917-0.

(25) Gnannt, F.; Gerwien, A.; Waldmannstetter, S.; Gracheva, S.; Dube, H. Directional Bias in Molecular Photogearing Evidenced by LED-Coupled Chiral Cryo-HPLC. *Angew. Chem. Int. Ed.* **2024**, *63* (38), e202405299. https://doi.org/10.1002/anie.202405299.

(26) Wiedbrauk, S.; Bartelmann, T.; Thumser, S.; Mayer, P.; Dube, H. Simultaneous Complementary Photoswitching of Hemithioindigo Tweezers for Dynamic Guest Relocalization. *Nat. Commun.* **2018**, *9* (1), 1456. https://doi.org/10.1038/s41467-018-03912-7.

(27) Grill, K.; Dube, H. Supramolecular Relay-Control of Organocatalysis with a Hemithioindigo-Based Molecular Motor. *J. Am. Chem. Soc.* **2020**, *142* (45), 19300–19307. https://doi.org/10.1021/jacs.0c09519.

(28) Dube, H.; Rebek Jr., J. Selective Guest Exchange in Encapsulation Complexes Using Light of Different Wavelenghts. *Angew. Chem. Int. Ed.* **2012**, *51* (13), 3207–3210. https://doi.org/10.1002/anie.201108074.

(29) Tanaka, K.; Taguchi, K.; Iwata, S.; Irie, T. Application of Benzoyl-Substituted Hemithioindigo as a Molecular Switch in Porphyrin-Quinone Recognition. *Supramol. Chem.* **2005**, *17* (8), 637–642. https://doi.org/10.1080/10610270500148036.

(30) Tanaka, K.; Kohayakawa, K.; Iwata, S.; Irie, T. Application of 2-Pyridyl-Substituted Hemithioindigo as a Molecular Switch in Hydrogen-Bonded Porphyrins. *J. Org. Chem.* **2008**, *73* (10), 3768–3774. https://doi.org/10.1021/jo800091d.

(31) Kink, F.; Collado, M. P.; Wiedbrauk, S.; Mayer, P.; Dube, H. Bistable Photoswitching of Hemithioindigo with Green and Red Light: Entry Point to Advanced Molecular Digital Information Processing. *Chem. – Eur. J.* **2017**, *23* (26), 6237–6243. https://doi.org/10.1002/chem.201700826.

(32) Zitzmann, M.; Hampel, F.; Dube, H. A Cross-Conjugation Approach for High-Performance Diaryl-Hemithioindigo Photoswitches. *Chem. Sci.* **2023**, *14* (21), 5734–5742. https://doi.org/10.1039/D2SC06939C.

(33) Herre, S.; Schadendorf, T.; Ivanov, I.; Herrberger, C.; Steinle, W.; Rück-Braun, K.; Preissner, R.; Kuhn, H. Photoactivation of an Inhibitor of the 12/15-Lipoxygenase Pathway. *ChemBioChem* **2006**, *7* (7), 1089–1095. https://doi.org/10.1002/cbic.200600082.

(34) Sailer, A.; Ermer, F.; Kraus, Y.; Lutter, F. H.; Donau, C.; Bremerich, M.; Ahlfeld, J.; Thorn-Seshold, O. Hemithioindigos for Cellular Photopharmacology: Desymmetrised Molecular Switch Scaffolds Enabling Design Control over the Isomer-Dependency of Potent Antimitotic Bioactivity. *ChemBioChem* **2019**, *20* (10), 1305–1314. https://doi.org/10.1002/cbic.201800752.

(35) Sailer, A.; Meiring, J. C. M.; Heise, C.; Pettersson, L. N.; Akhmanova, A.; Thorn-Seshold, J.; Thorn-Seshold, O. Pyrrole Hemithioindigo Antimitotics with Near-Quantitative Bidirectional Photoswitching That Photocontrol Cellular Microtubule Dynamics with Single-Cell Precision. *Angew. Chem. Int. Ed.* **2021**, *60* (44), 23695–23704. https://doi.org/10.1002/anie.202104794.

(36) Köttner, L.; Wolff, F.; Mayer, P.; Zanin, E.; Dube, H. Rhodanine-Based Chromophores: Fast Access to Capable Photoswitches and Application in Light-Induced Apoptosis. *J. Am. Chem. Soc.* **2024**, *146* (3), 1894–1903. https://doi.org/10.1021/jacs.3c07710.

(37) Hoffmann, K.; Mayer, P.; Dube, H. A Hemithioindigo Molecular Motor for Metal Surface Attachment. *Org. Biomol. Chem.* **2019**, *17* (7), 1979–1983. https://doi.org/10.1039/C8OB02424C.

(38) Seki, T.; Tamaki, T.; Yamaguchi, T.; Ichimura, K. Photochromism of Hemithioindigo Derivatives. II. Photochromic Behaviors in Bilayer Membranes and Related Systems. *Bull. Chem. Soc. Jpn.* **1992**, *65* (3), 657–663. https://doi.org/10.1246/bcsj.65.657.

(39) Eggers, K.; Fyles, T. M.; Montoya-Pelaez, P. J. Synthesis and Characterization of Photoswitchable Lipids Containing Hemithioindigo Chromophores. *J. Org. Chem.* **2001**, *66* (9), 2966–2977. https://doi.org/10.1021/jo0056848.

(40) Cordes, T.; Schadendorf, T.; Rück-Braun, K.; Zinth, W. Chemical Control of Hemithioindigo-Photoisomerization – Substituent-Effects on Different Molecular Parts. *Chem. Phys. Lett.* **2008**, *455* (4), 197–201. https://doi.org/10.1016/j.cplett.2008.02.096.

(41) Graupner, F. F.; Herzog, T. T.; Rott, F.; Oesterling, S.; de Vivie-Riedle, R.; Cordes, T.; Zinth, W. Photoisomerization of Hemithioindigo Compounds: Combining Solvent- and Substituent- Effects into an Advanced Reaction Model. *Chem. Phys.* **2018**, *515*, 614–621. https://doi.org/10.1016/j.chemphys.2018.07.043.

(42) Wiedbrauk, S.; Maerz, B.; Samoylova, E.; Reiner, A.; Trommer, F.; Mayer, P.; Zinth, W.; Dube, H. Twisted Hemithioindigo Photoswitches: Solvent Polarity Determines the Type of Light-Induced Rotations. *J. Am. Chem. Soc.* **2016**, *138* (37), 12219–12227. https://doi.org/10.1021/jacs.6b05981.

(43) Fischer, T.; Leitner, J.; Gerwien, A.; Mayer, P.; Dreuw, A.; Dube, H.; Wachtveitl, J. Mechanistic Elucidation of the Hula-Twist Photoreaction in Hemithioindigo. *J. Am. Chem. Soc.* **2023**, *145* (27), 14811–14822. https://doi.org/10.1021/jacs.3c03536.

(44) Wiedbrauk, S.; Maerz, B.; Samoylova, E.; Mayer, P.; Zinth, W.; Dube, H. Ingredients to TICT Formation in Donor Substituted Hemithioindigo. *J. Phys. Chem. Lett.* **2017**, *8* (7), 1585–1592. https://doi.org/10.1021/acs.jpclett.7b00371.

(45) Wilcken, R.; Schildhauer, M.; Rott, F.; Huber, L. A.; Guentner, M.; Thumser, S.; Hoffmann, K.; Oesterling, S.; de Vivie-Riedle, R.; Riedle, E.; Dube, H. Complete Mechanism of Hemithioindigo Motor Rotation. *J. Am. Chem. Soc.* **2018**, *140* (15), 5311–5318. https://doi.org/10.1021/jacs.8b02349.

(46) Schildhauer, M.; Rott, F.; Thumser, S.; Mayer, P.; de Vivie-Riedle, R.; Dube, H. A Prospective Ultrafast Hemithioindigo Molecular Motor. *ChemPhotoChem* **2019**, *3* (6), 365–371. https://doi.org/10.1002/cptc.201900074.

(47) Wilcken, R.; Huber, L.; Grill, K.; Guentner, M.; Schildhauer, M.; Thumser, S.; Riedle, E.; Dube, H. Tuning the Ground and Excited State Dynamics of Hemithioindigo Molecular Motors by Changing Substituents. *Chem. – Eur. J.* **2020**, *26* (59), 13507–13512. https://doi.org/10.1002/chem.202003096.

(48) Plötner, J.; Dreuw, A. Molecular Mechanism of the Z/E-Photoisomerization of Hemithioindigo Hemistilbene. *J. Phys. Chem. A* **2009**, *113* (43), 11882–11887. https://doi.org/10.1021/jp903156j.

(49) Nenov, A.; Cordes, T.; Herzog, T. T.; Zinth, W.; de Vivie-Riedle, R. Molecular Driving Forces for Z/E Isomerization Mediated by Heteroatoms: The Example Hemithioindigo. *J. Phys. Chem. A* **2010**, *114* (50), 13016–13030. https://doi.org/10.1021/jp107899g.

(50) Yang, M.; Huo, C.; Li, A.; Lei, Y.; Yu, L.; Zhu, C. Excited-State E → Z Photoisomerization Mechanism Unveiled by Ab Initio Nonadiabatic Molecular Dynamics Simulation for Hemithioindigo–Hemistilbene. *Phys. Chem. Chem. Phys.* **2017**, *19* (19), 12185–12198. https://doi.org/10.1039/C7CP00102A.

(51) Lea, M. R.; Stavros, V. G.; Maurer, R. J. Effect of Electron Donating/Withdrawing Groups on Molecular Photoswitching of Functionalized Hemithioindigo Derivatives: A Computational Multireference Study. *ChemPhotoChem* **2022**, *6* (7), e202100290. https://doi.org/10.1002/cptc.202100290.

(52) Liu, R. S.; Asato, A. E. The Primary Process of Vision and the Structure of Bathorhodopsin: A Mechanism for Photoisomerization of Polyenes. *Proc. Natl. Acad. Sci.* **1985**, *82* (2), 259–263. https://doi.org/10.1073/pnas.82.2.259.

(53) Gerwien, A.; Schildhauer, M.; Thumser, S.; Mayer, P.; Dube, H. Direct Evidence for Hula Twist and Single-Bond Rotation Photoproducts. *Nat. Commun.* **2018**, *9* (1), 2510. https://doi.org/10.1038/s41467-018-04928-9.

(54) Gerwien, A.; Jehle, B.; Irmler, M.; Mayer, P.; Dube, H. An Eight-State Molecular Sequential Switch Featuring a Dual Single-Bond Rotation Photoreaction. *J. Am. Chem. Soc.* **2022**, *144* (7), 3029–3038. https://doi.org/10.1021/jacs.1c11183.

(55) Meltzer, C.; Paul, J.; Dietrich, H.; Jäger, C. M.; Clark, T.; Zahn, D.; Braunschweig, B.; Peukert, W. Indentation and Self-Healing Mechanisms of a Self-Assembled Monolayer—A Combined Experimental and Modeling Study. *J. Am. Chem. Soc.* **2014**, *136* (30), 10718–10727. https://doi.org/10.1021/ja5048076.

(56) Dietrich, H.; Scheiner, S.; Portilla, L.; Zahn, D.; Halik, M. Improving the Performance of Organic Thin-Film Transistors by Ion Doping of Ethylene-Glycol-Based Self-

Assembled Monolayer Hybrid Dielectrics. *Adv. Mater.* **2015**, *27* (48), 8023–8027. https://doi.org/10.1002/adma.201503911.

(57) Barbatti, M. Nonadiabatic Dynamics with Trajectory Surface Hopping Method. *WIREs Comput. Mol. Sci.* **2011**, *1* (4), 620–633. https://doi.org/10.1002/wcms.64.

(58) Fabiano, E.; Keal, T. W.; Thiel, W. Implementation of Surface Hopping Molecular Dynamics Using Semiempirical Methods. *Chem. Phys.* **2008**, *349* (1), 334–347. https://doi.org/10.1016/j.chemphys.2008.01.044.

(59) Duchstein, P.; Neiss, C.; Görling, A.; Zahn, D. Molecular Mechanics Modeling of Azobenzene-Based Photoswitches. *J. Mol. Model.* **2012**, *18* (6), 2479–2482. https://doi.org/10.1007/s00894-011-1270-6.

(60) Neese, F.; Wennmohs, F.; Becker, U.; Riplinger, C. The ORCA Quantum Chemistry Program Package. *J. Chem. Phys.* **2020**, *152* (22), 224108. https://doi.org/10.1063/5.0004608.

(61) Neese, F. Software Update: The ORCA Program System—Version 5.0. *WIREs Comput. Mol. Sci.* **2022**, *12* (5), e1606. https://doi.org/10.1002/wcms.1606.

(62) Stephens, P. J.; Devlin, F. J.; Chabalowski, C. F.; Frisch, M. J. Ab Initio Calculation of Vibrational Absorption and Circular Dichroism Spectra Using Density Functional Force Fields. *J. Phys. Chem.* **1994**, *98* (45), 11623–11627. https://doi.org/10.1021/j100096a001.

(63) Weigend, F.; Ahlrichs, R. Balanced Basis Sets of Split Valence, Triple Zeta Valence and Quadruple Zeta Valence Quality for H to Rn: Design and Assessment of Accuracy. *Phys. Chem. Chem. Phys.* **2005**, *7* (18), 3297–3305. https://doi.org/10.1039/B508541A.

(64) Weigend, F. Accurate Coulomb-Fitting Basis Sets for H to Rn. *Phys. Chem. Chem. Phys.* **2006**, *8* (9), 1057–1065. https://doi.org/10.1039/B515623H.

(65) Grimme, S.; Antony, J.; Ehrlich, S.; Krieg, H. A Consistent and Accurate Ab Initio Parametrization of Density Functional Dispersion Correction (DFT-D) for the 94 Elements H-Pu. *J. Chem. Phys.* **2010**, *132* (15), 154104. https://doi.org/10.1063/1.3382344.

(66) Grimme, S.; Ehrlich, S.; Goerigk, L. Effect of the Damping Function in Dispersion Corrected Density Functional Theory. *J. Comput. Chem.* **2011**, *32* (7), 1456–1465. https://doi.org/10.1002/jcc.21759.

(67) Kendall, R. A.; Früchtl, H. A. The Impact of the Resolution of the Identity Approximate Integral Method on Modern Ab Initio Algorithm Development. *Theor. Chem. Acc.* **1997**, *97* (1), 158–163. https://doi.org/10.1007/s002140050249.

(68) Neese, F.; Wennmohs, F.; Hansen, A.; Becker, U. Efficient, Approximate and Parallel Hartree–Fock and Hybrid DFT Calculations. A 'Chain-of-Spheres' Algorithm for the Hartree–Fock Exchange. *Chem. Phys.* **2009**, *356* (1), 98–109. https://doi.org/10.1016/j.chemphys.2008.10.036.

(69) Wang, J.; Wolf, R. M.; Caldwell, J. W.; Kollman, P. A.; Case, D. A. Development and Testing of a General Amber Force Field. *J. Comput. Chem.* **2004**, *25* (9), 1157–1174. https://doi.org/10.1002/jcc.20035.

(70) Case, D. A.; Aktulga, H. M.; Belfon, K.; Ben-Shalom, I. Y.; Berryman, J. T.; Brozell, S. R.; Cerutti, D. S.; Cheatham, T. E.; Cisneros, G. A.; Cruzeiro, V. W. D.; Darden, T. A.; Duke, R. E.; Giambasu, G.; Gilson, M. K.; Gohlke, H.; Goetz, A. W.; Harris, R.; Izadi, S.; Izmailov, S. A.; Kasavajhala, K.; Kaymak, M. C.; King, E.; Kovalenko, A.; Kurtzman, T.; Lee, T. S.; LeGrand, S.; Li, P.; Lin, C.; Liu, J.; Luchko, T.; Luo, R.; Machado, M.; Man,

V.; Manathunga, M.; Merz, K. M.; Miao, Y.; Mikhailovskii, O.; Monard, G.; Nguyen, H.; O'Hearn, K. A.; Onufriev, A.; Pan, F.; Pantano, S.; Qi, S.; Rahnamoun, A.; Roe, D. R.; Roitberg, A.; Sagui, C.; Schott-Verdugo, S.; Shajan, A.; Shen, J.; Simmerling, C. L.; Skrynnikov, N. R.; Smith, J.; Swails, J.; Walker, R. C.; Wang, J.; Wang, J.; Wei, H.; Wolf, R. M.; Wu, X.; Xiong, Y.; Xue, Y.; York, D. M.; Zhao, S.; Kollman, P. A. Amber 2022, 2022.

(71) Bayly, C. I.; Cieplak, P.; Cornell, W.; Kollman, P. A. A Well-Behaved Electrostatic Potential Based Method Using Charge Restraints for Deriving Atomic Charges: The RESP Model. *J. Phys. Chem.* **1993**, *97* (40), 10269–10280. https://doi.org/10.1021/j100142a004.

(72) Rassolov, V. A.; Ratner, M. A.; Pople, J. A.; Redfern, P. C.; Curtiss, L. A. 6-31G* Basis Set for Third-Row Atoms. *J. Comput. Chem.* **2001**, *22* (9), 976–984. https://doi.org/10.1002/jcc.1058.

(73) Francl, M. M.; Pietro, W. J.; Hehre, W. J.; Binkley, J. S.; Gordon, M. S.; DeFrees, D. J.; Pople, J. A. Self-consistent Molecular Orbital Methods. XXIII. A Polarization-type Basis Set for Second-row Elements. *J. Chem. Phys.* **1982**, *77* (7), 3654–3665. https://doi.org/10.1063/1.444267.

(74) Ditchfield, R.; Hehre, W. J.; Pople, J. A. Self-Consistent Molecular-Orbital Methods. IX. An Extended Gaussian-Type Basis for Molecular-Orbital Studies of Organic Molecules. *J. Chem. Phys.* **1971**, *54* (2), 724–728. https://doi.org/10.1063/1.1674902.

(75) Hehre, W. J.; Ditchfield, R.; Pople, J. A. Self—Consistent Molecular Orbital Methods. XII. Further Extensions of Gaussian—Type Basis Sets for Use in Molecular Orbital Studies of Organic Molecules. *J. Chem. Phys.* **1972**, *56* (5), 2257–2261. https://doi.org/10.1063/1.1677527.

(76) Hariharan, P. C.; Pople, J. A. The Influence of Polarization Functions on Molecular Orbital Hydrogenation Energies. *Theor. Chim. Acta* **1973**, *28* (3), 213–222. https://doi.org/10.1007/BF00533485.

(77) Frisch, M. J.; Trucks, G. W.; Schlegel, H. B.; Scuseria, G. E.; Robb, M. A.; Cheeseman, J. R.; Scalmani, G.; Barone, V.; Petersson, G. A.; Nakatsuji, H.; Li, X.; Caricato, M.; Marenich, A. V.; Bloino, J.; Janesko, B. G.; Gomperts, R.; Mennucci, B.; Hratchian, H. P.; Ortiz, J. V.; Izmaylov, A. F.; Sonnenberg, J. L.; Williams-Young, D.; Ding, F.; Lipparini, F.; Egidi, F.; Goings, J.; Peng, B.; Petrone, A.; Henderson, T.; Ranasinghe, D.; Zakrzewski, V. G.; Gao, J.; Rega, N.; Zheng, G.; Liang, W.; Hada, M.; Ehara, M.; Toyota, K.; Fukuda, R.; Hasegawa, J.; Ishida, M.; Nakajima, T.; Honda, Y.; Kitao, O.; Nakai, H.; Vreven, T.; Throssell, K.; Montgomery, J. A., Jr.; Peralta, J. E.; Ogliaro, F.; Bearpark, M. J.; Heyd, J. J.; Brothers, E. N.; Kudin, K. N.; Staroverov, V. N.; Keith, T. A.; Kobayashi, R.; Normand, J.; Raghavachari, K.; Rendell, A. P.; Burant, J. C.; Iyengar, S. S.; Tomasi, J.; Cossi, M.; Millam, J. M.; Klene, M.; Adamo, C.; Cammi, R.; Ochterski, J. W.; Martin, R. L.; Morokuma, K.; Farkas, O.; Foresman, J. B.; Fox, D. J. Gaussian˜16 Revision A.03, 2016.

(78) Wang, J.; Wang, W.; Kollman, P. A.; Case, D. A. Automatic Atom Type and Bond Type Perception in Molecular Mechanical Calculations. *J. Mol. Graph. Model.* **2006**, *25* (2), 247–260. https://doi.org/10.1016/j.jmgm.2005.12.005.

(79) Thompson, A. P.; Aktulga, H. M.; Berger, R.; Bolintineanu, D. S.; Brown, W. M.; Crozier, P. S.; in 't Veld, P. J.; Kohlmeyer, A.; Moore, S. G.; Nguyen, T. D.; Shan, R.; Stevens, M. J.; Tranchida, J.; Trott, C.; Plimpton, S. J. LAMMPS - a Flexible Simulation Tool for Particle-Based Materials Modeling at the Atomic, Meso, and Continuum Scales.

Comput. Phys. Commun. **2022**, *271*, 108171. https://doi.org/10.1016/j.cpc.2021.108171.

(80) Pedregosa, F.; Varoquaux, G.; Gramfort, A.; Michel, V.; Thirion, B.; Grisel, O.; Blondel, M.; Prettenhofer, P.; Weiss, R.; Dubourg, V.; Vanderplas, J.; Passos, A.; Cournapeau, D.; Brucher, M.; Perrot, M.; Duchesnay, É. Scikit-Learn: Machine Learning in Python. *J. Mach. Learn. Res.* **2011**, *12* (85), 2825–2830.

(81) Polonius, S.; Lehrner, D.; González, L.; Mai, S. Resolving Photoinduced Femtosecond Three-Dimensional Solute–Solvent Dynamics through Surface Hopping Simulations. *J. Chem. Theory Comput.* **2024**, *20* (11), 4738–4750. https://doi.org/10.1021/acs.jctc.4c00169.